ADVANCED ELECTRONIC MATERIALS Open Access
www.advelectronicmat.de

# High-Density Flexible Neural Implants with Submicron Feedline Resolution

*Lina Koschinski, Thomas Grap, Erkan Yilmaz, Marius Kleutgens, Simon Decke, Martin Kasavetov, Marie Jung, Alejandro Carnicer-Lombarte, George Malliaras, Andreas Offenhäusser, and Viviana Rincón Montes**

**The development of high-density microelectrode arrays (MEAs) for large-scale brain recordings requires neural probes with reduced footprints to minimize tissue damage. One way to achieve this is by implementing dense electrode arrays with narrower feedline dimensions, though this increases susceptibility to capacitive coupling between electrical interconnects. To address this, this study explores the resolution limits for high-density flexible MEAs by optimizing the fabrication using optical contact lithography (OCL) and electron beam lithography (EBL). OCL enables metal feedlines with widths of 520 nm and interconnect spaces of 280 nm, while EBL allows the realization of 50 nm feedlines with 150 nm spaces on flexible parylene C substrates. Based on these techniques, we fabricate a flexible 64-channel intracortical implant with a miniaturized cross-section of only 50 × 6 or 70 × 6 μm$^2$. In vivo validation in awake rats demonstrates that the fabricated, high-density flexible intracortical implants with submicron feedline resolution offer low-impedance electrodes and reduced crosstalk, enabling reliable neuronal recordings. These findings demonstrate the feasibility of miniaturizing flexible MEAs using a single-metal layer process, thereby reducing manufacturing complexity in high-density thin-film polymer-based neural interfaces.**

## 1. Introduction

Neural implants have emerged as powerful tools in neuroscience and neurology, enabling neural decoding and modulation. Widely used in basic research and pre-clinical and clinical settings, they allow for the understanding of neural function in both healthy and diseased conditions, as well as for the investigation and implementation of new therapies for the restoration of lost sensorimotor functions.[1,2] Often incorporating microelectrode arrays (MEAs), neural implants interface neural structures electrically. These devices allow neural activity to be recorded by measuring electrical potentials, including local field potentials (LFPs) – low-frequency signals that reflect the summed activity of neuronal populations – and action potentials (APs) – high-frequency signals that reflect the activity of individual neurons. Additionally, they allow neural activity to be modulated by the delivery of electrical pulses.

Despite the advancement provided by neural implants, foreign body reactions (FBRs) and inflammation responses are triggered due to neuronal loss upon implantation and the mechanical mismatch between the materials of the implant and the tissue, causing implant failure due to glial scarring tissue.[3–5] Accordingly, biomimetic approaches such as designs with neuron-like dimensions and miniaturized cross-sections,[6–8] and flexible, soft interfaces,[9–11] have been proposed to reduce implantation footprints and FBRs. However, device

L. Koschinski, E. Yilmaz, M. Kleutgens, S. Decke, M. Kasavetov, M. Jung, A. Offenhäusser, V. Rincón Montes
Bioelectronics
Institute of Biological Information Processing-3
Forschungszentrum Jülich
52428 Jülich, Germany
E-mail: v.rincon.montes@fz-juelich.de

The ORCID identification number(s) for the author(s) of this article can be found under https://doi.org/10.1002/aelm.202500088



**DOI: 10.1002/aelm.202500088**

L. Koschinski, S. Decke, M. Jung
RWTH Aachen University
52062 Aachen, Germany

L. Koschinski, T. Grap
Helmholtz Nano Facility (HNF)
Forschungszentrum Jülich
52428 Jülich, Germany

M. Kleutgens
FH Aachen
University of Applied Sciences
52066 Jülich, Germany

A. Carnicer-Lombarte, G. Malliaras, V. Rincón Montes
Bioelectronics Laboratory
University of Cambridge
CB3 0FA Cambridge, UK

miniaturization has limited the spatial resolution of implants, particularly those comprising penetrating structures for intracortical use, by restricting the number of electrical contacts or electrodes that can fit per implant shank (also known as shafts or threads).[5]

The pursuit of large-scale intracortical recordings requires high-density electrode arrays capable of capturing APs from every neuron involved in a given neural circuit. This requirement translates into the need for multiple electrodes per shank and multiple shanks to effectively map brain activity. However, increasing the electrode count inherently involves incorporating active electronics, such as a selectable switching matrix,[12] or, for passive elements, dedicating one feedline per electrode. Both approaches contribute to an increase in the cross-sectional area of the implant, which can cause more tissue damage. Silicon technology has made it possible to fabricate high-density neural probes, with penetrating shanks with up to 1280 electrodes through active electronic integration.[12] However, their cross-sectional footprint (24 μm × 70 μm) is still well above that of polymer-based penetrating shanks with the highest density and smallest footprint (32 electrodes, 4–6 μm × 50 μm).[13] Various approaches have been taken to reduce the size of the implant and thus minimize tissue damage (Table ST1, Supporting Information). One is to use micrometer-scale feedlines with multiple metal layers, allowing an increase in the electrode count while maintaining narrow shank widths.[4,13,14] Alternatively, feedlines can be miniaturized in the sub-micron range, an approach that requires the exploration and implementation of lithographic techniques that go beyond standard optical contact lithography (OCL), such as maskless, electron-beam lithography (EBL), and deep UV lithography.[6,13,15]

While both approaches have proven useful in increasing the electrode density of flexible neural implants, the incorporation of multiple metal layers introduces greater microfabrication complexity compared to single-layer processes. Additionally, the superposition of feedlines can contribute to varying degrees of crosstalk, depending on factors such as the choice of insulation material and its thickness. On the other hand, reducing the dimensions of the feedlines increases the lead resistance of the electrical contacts and the risk of crosstalk. Furthermore, while EBL offers unmatched resolution, its processing time is slower and more expensive than UV and deep UV techniques, the latter being an industry standard. Therefore, a trade-off between lead resistance, the dimensional footprint of the implant, microfabrication resolution, and process time is critical for microfabrication feasibility, scalability, and affordability (Table ST2, Supporting Information).

In this work, we developed a high-density intracortical neural implant featuring sub-micron feedlines and minimized cross-sectional dimensions. To achieve this, we investigated the resolution limits of both OCL and EBL and established a process flow for the microfabrication of high-density flexible penetrating neural probes using parylene-C (PaC). Following crosstalk simulations and optimization of the microfabrication process, we successfully fabricated a single-metal-layer high-density implant with one intracortical shank housing 64 electrodes and a compact footprint of 6 μm × 50–70 μm. Finally, the functionality of the implant was validated in awake, freely moving rodents.

## 2. Experimental Section

### 2.1. Fabrication of Flexible Neural Probes

Single-metal layer high-density flexible implants with sub-micron feedline resolution were fabricated as follows (**Figure 1A**). Microfabrication was performed on a 4-inch silicon host wafer (Figure 1Ai) coated with a 3 μm thick PaC layer (PDS 2010 LABCOTER 2, Specialty Coating Systems Inc.; with a coating base pressure of 15 mTorr, an operating/deposition pressure of 25 mTorr, and a vaporizer temperature of 160 °C) (Figure 1Aii). Metal feedlines, electrodes, and contact pads were then patterned using OCL or EBL (Figure 1Aiii), followed by metallization and a lift-off process (Figure 1Aiv). A second 3 μm PaC layer was deposited as encapsulation or passivation (Figure 1Av). Finally, the shape, electrode- and contact-pads-openings were patterned using a positive photoresist etch mask by maskless lithography (MLA 150, Heidelberg Instruments, Germany) (Figure 1Avi) and a dry etching step using reactive ion etching (Figure 1Avii) (Plasmalab 100 ICP180, Oxford Instruments, Abingdon), as described previously.[8] The microfabrication processes were carried out in the laboratories of the Institute of Biological Information Processing -3 (Bioelectronics) and the Helmholtz Nano Facility at the *Forschungszentrum* Jülich.[16]

#### *2.1.1. Optical Contact Lithography-Based High-Density and Sub-Micron Structures*

The resolution limits of OCL were explored using the mask aligner MA8BA8-Gen3 (SÜSS MicroTec, Germany) to achieve sub-micron feature resolution. After the deposition of the first PaC layer, the feedlines were patterned using a lift-off process. Prior to spin-coating the masking photoresist, the wafer was dehydrated at 150 °C for 5 min on a hot plate (Gestigkeit Typ ET, Harry Gestigkeit GmbH, Germany). Subsequently, AZ LNR003 (MicroChemcicals GmbH, Germany) was diluted with AZ EBR (MicroChemicals GmbH, Germany) in a volume ratio of 2:1, respectively, and spin-coated for 45 s at 4000 rpm. After spin-coating (LabSpin 8, SÜSS MicroTec, Germany), the coated wafer was soft-baked on a direct contact hot plate at 120 °C for 2 min. UV exposure was then performed under vacuum contact with a dose of 65 mJ $cm^{-2}$. The wafer was then processed at 100 °C for 90 s for post-exposure bake. The structures were developed in AZ MIF326 (MicroChemicals GmbH, Germany) for 30 s and stopped in a water cascade bath. After spin-drying, the metallization of 20 nm titanium and 100 nm gold was performed in an electron-beam assisted evaporator (Pfeiffer PLS 570, Germany). The metal on the resist was then lifted in an 80 °C NI555 (MicroChemicals GmbH, Germany) bath for 3 hours. The wafer was then rinsed in acetone and isopropanol for 2 min each.

#### *2.1.2. Electron-Beam Lithography (EBL)-Based High-Density Neural Implants*

As with the OCL-based process, the fabrication of the EBL-based process started with a Si host wafer coated with a 3 μm PaC layer. After a dehydration step, the resist was spin-coated. A two-layer

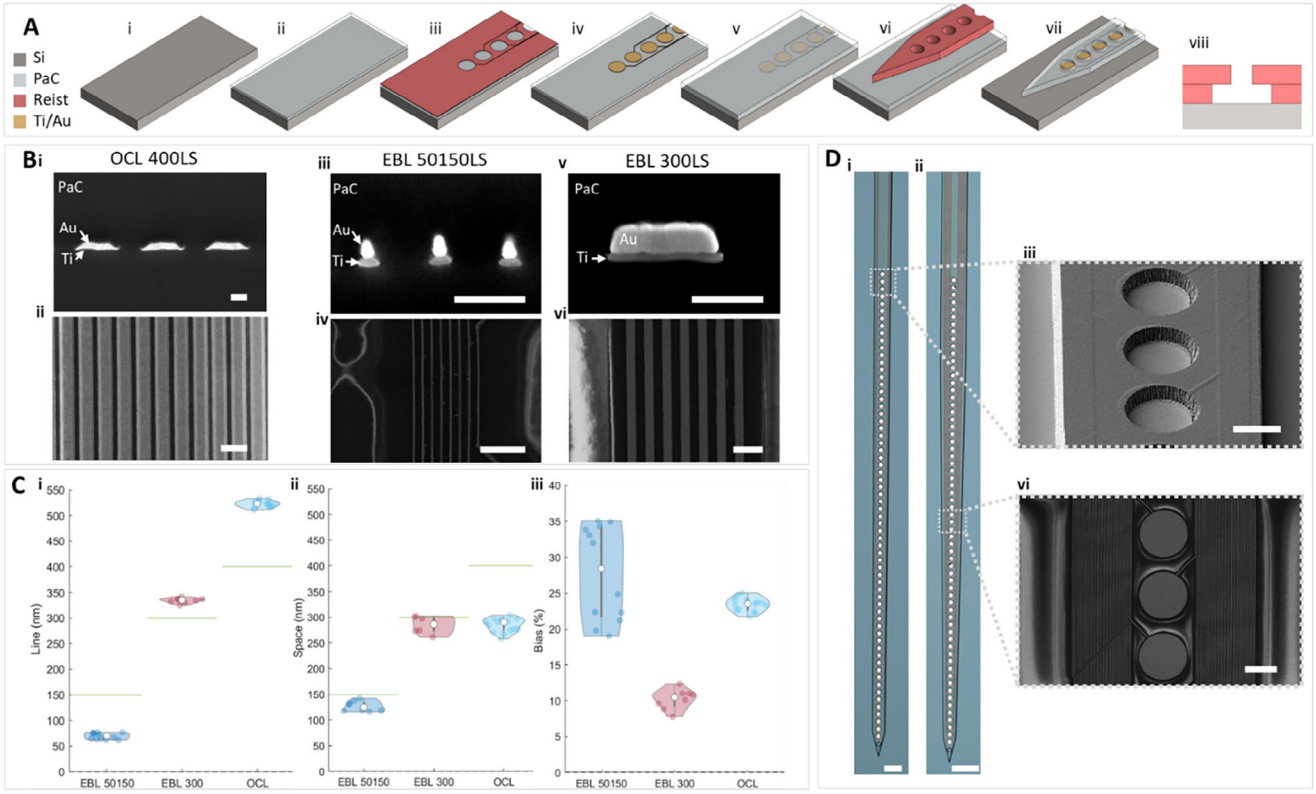


**Figure 1.** Lithographic resolution and microfabrication of high-density intracortical probes with submicron feedline resolution. A) Schematic of microfabrication process-flow of high-density intracortical probes: host silicon substrate (Ai), PaC-coating (Aii), feedline lithography (Aiii), metallization and lift off (Aiv), PaC passivation (Av), lithography for the shape and electrode openings (Avi) and finalized sample after RIE but still on the host wafer (Avii). The EBL resist layer stack of PMMA (617.03 and 679.03) is schematically presented in Aviii). B) Focused-ion beam (FIB) cuts (upper row, Bi, Biii, Bv, scale bar 200 nm) and scanning electron microscopy (SEM) images (lower row, Bii, Biv, Bvi, scale bar 1 µm) with feedline variations of 50/150 nm lines and spaces (EBL 50150LS, left) and 300 nm lines and spaces (EBL 300LS middle) using EBL, and 400 nm lines and spaces (OCL 400LS, right) using OCL. C) Dimensional measurements of lines (Ci) and spaces (Cii), along with their calculated critical dimension bias in % (Ciii) from FIB-cuts (measured feedlines and spaces: n = 15). Aim of dimension of lines or space is marked with green line. D) Microscope picture of finalized neural implants 50150LS (Di, scale bar 50 µm) and 300LS (Dii, scale bar 70 µm). SEM image of finalized 50150LS neural implant in an angled view with zoom to the electrode openings (Diii, scale bar 10 µm). SEM image of the 300LS feedlines and electrodes from top view (at the process step after lift-off (Aiv)) (Dvi, scale bar 10 µm).

photoresist stack of a copolymer and PMMA (both from Allresist GmbH, Germany,)[17,18] was used for the lift-off process.[19] The copolymer AR-P 617.03 was first spin-coated for 45 s at 3000 rpm to create a suitable undercut. The resist was baked at 150 °C for 5 min before spin-coating with PMMA AR-P 679.03 for 45 s at 2000 rpm. This was followed by a bake at 150 °C for 5 min. EBL was then performed using an EBPG 5200 (Raith GmbH, Germany). To optimize the process, exposure doses ranging from $2 \times 500$ to $2 \times 930$ µC cm$^{-2}$ were tested to achieve varying structure sizes within a neural implant.

In this work, two different sizes of feedlines are focused to characterize the scaling of implant dimensions. The first layout consisted of feedlines with 300 nm lines and spacing (300 LS – lines and spaces), while the second layout contained feedlines with a width of 50 nm and a spacing of 150 nm (50/150 LS). To increase the contrast of the resist, the developer AR 600–55 (Allresist GmbH) was cooled down to 0 °C with an MX7LR-20 bath (VWR North, Germany), and the wafer was developed for 30 s.[20,21] To stop the development, the wafer was transferred directly into a hexane bath at room temperature for 10 s and air-dried with nitrogen. Subsequently, 20 nm of titanium and 100 nm of gold were deposited in an e-beam-assisted evaporator (Univex 400, Leybold, Germany). The lift-off of the metal stack was performed in an acetone bath for 3 h, cleaned in a second bath for 2 min, and rinsed in isopropanol for an additional 2 min. The structures were encapsulated with a second 3 µm PaC layer.

In both cases, the wafer was again patterned with AZ 4562 resist (MicroChemicals, Germany) to create the shape and electrode as well as the contact pad openings. This was followed by a reactive ion etching step using a gas mixture of oxygen ($O_2$, 36 sccm) and tetrafluoromethane ($CF_4$, 4 sccm), and a RF/ICP power of 50/500 W with a strike pressure of 0.03 mbar. The photoresist was stripped with AZ 100 remover in a two-bath system using low-powered ultrasound and finally rinsed in isopropanol in a three-bath system. This etching step enabled the removal of PaC at the electrode and contact pad openings while simultaneously defining the implant outline, reducing processing time, and minimizing potential misalignments. Although the gold layer was partially etched during this process, ≈40–50 nm remained, which was subsequently coated with PEDOT:PSS

 

in a post-processing step to reduce the impedance of the electrodes.

#### 2.1.3. Packaging

To release the samples from the host wafer, the finished implants were carefully peeled off with a drop of deionized water, and then manually flip-chip bonded onto a customized 64-channel printed circuit board (PCB). The 64-channel PCB held two 36-channel Omnetics connectors (A79026-001, Omnetics Corp, USA) pre-soldered to the PCB. For flip-chip bonding the PCB was heated to 180 °C on a hot plate to allow the solder paste (SMDLTB35T4, Chip Quik, Sn60/Bi40) to be applied. After the alloy had formed liquid bumps on the contact pads, the peeled-off implants were flipped, manually aligned with the PCB, and cooled down to room temperature. Medical grade UV-curable glue (Vitralit 7311 FO, Panacol-Elosol GmbH, Germany) was applied to seal the connector-implant interface.

#### 2.1.4. Electrodeposition of PEDOT:PSS

PEDOT:PSS was electrodeposited as a coating on the gold electrodes. For this purpose, an EDOT:PSS solution was prepared containing 0.1% (w/v) of 3,4-ethylenedioxythiophene (EDOT) (Sigma Aldrich, Germany) and 0.7% poly(sodium 4-styrenesulfonate) (PSS) (Sigma Aldrich, Germany) in deionized water. To remove fabrication-related contaminants and residues, the gold electrodes were electrochemically cleaned. The electrodes were then short-circuited, immersed in 0.1 M PBS, and subjected to ten cyclic voltammetry (CV) cycles (−0.6 to 0.9 V, 100 mV $s^{-1}$) with a VSP-300 potentiostat (Bio-Logic Science Instruments, France).[22] To clean the electrodes from organic contaminants,[23] the implants were then exposed to an $O_2$ plasma treatment with a pressure of 0.8 mbar, a power of 80 W, and a duration of 3 min (Pico Low Pressure Plasma System, Electronic Diener GmbH & Co. KG, Germany). Subsequently, electropolymerization of PEDOT:PSS (Poly-(2,3-dihydrothieno-1,4-dioxin)-poly-(styrolsulfonat)) via chronoamperometry using a constant potential of 1 V for 20 s was carried out on the gold electrodes. For all electrochemical processes, a three-electrode setup was used with a platinum wire and a silver-silver chloride electrode (kept in 3 M KCL, DRIREF-2, World Precision Instruments, USA) as counter and reference, respectively. After each electrochemical step, the probes were rinsed with deionized water. This process is based on previous reports, which resulted in a PEDOT:PSS coating ≈560 nm thick.[22]

#### 2.1.5. Insertion Shuttle

Following the packaging process, the implants were cleaned in deionized water and sterilized in 70% ethanol. Subsequently, a 50 µm-in-diameter tungsten rod was temporarily affixed to the flexible shank of each probe using a mixture of polyethylene glycol (PEG 8000, Sigma Aldrich, Germany) in deionized water in a ratio of 15% w/w prepared at room temperature. After applying the PEG mixture, the implants were air-dried at room temperature overnight.

### 2.2. Electrical Characterization

#### 2.2.1. Crosstalk Simulation

Crosstalk was defined according to Equation (1), as the ratio of the root mean square (RMS) values[24] of the voltages at the *aggressor* and the *victim* feedline, where $U_{victim}$ denotes the RMS voltage measured at the affected, inactive feedline (victim, **Figure** 2B, green) and $U_{aggressor}$ represents the RMS voltage measured at the adjacent, active and thus in this case emitting feedline (aggressor, Figure 2B, orange).

$$Crosstalk = \frac{U_{victim}}{U_{aggresor}} \tag{1}$$

To design a simulation of crosstalk in the feedline structure, the boundary parameters need to be set. Therefore, an equivalent circuit is modeled and presented in Figure 2B. Here, a two-electrode configuration in phosphate buffered solution (0.1 M PBS, with a conductivity of $\sigma_{Ey} = 1.5$ S $m^{-1}$)[25] and relative permittivity of $\varepsilon_{Ey} = 80$)[26] is connected to a measurement system (in air). The input impedance of the measurement system onto each feedline is electrically represented as a resistance $R_M = 470$ MΩ with a parallel capacitance $C_M = 10$ pF connected to ground, in accordance with the datasheet specifications of a MCS-ME2100-HS32Ch-headstage (Multichannels Systems, Germany).[27] Stray capacitances from the Omnetics connector are not considered in this model. For the model of the implant, a 6 µm PaC encapsulation was applied around the feedlines, with a relative permittivity of $\varepsilon_{PaC} = 3.1$[28] and electrical conductivity of $\sigma_{PaC} =$ 1.136E-15 S/m.[29] The thickness of the gold feedlines was set in the simulation to 100 nm with a relative permittivity of $\varepsilon_{Au} =$ 6.9[30] and electrical conductivity of $\sigma_{Au} = 41.1E6$ S $m^{-1}$.[31,32] At the electrode-electrolyte interface, the electric double layer (EDL) was modeled using a simplified Randles circuit (Figure S1, Supporting Information), consisting of the electrolyte resistance ($R_{Ey}$, Figure 2A) in series to an R//C circuit, where the double-layer capacitance ($C_{EDL}$, Figure 2A) is parallel to the charge transfer resistance ($R_{EDL}$, Figure 2A). The values of the Randles circuit model were obtained by performing an impedance fit on exemplary impedance spectra of the high-density neural probes with PEDOT:PSS coated electrodes microfabricated in this work using the EC-lab software (BioLogic Science Instruments, France). Here, a constant phase element (CPE) was incorporated into the model:[33]

$$C = R_{CPE}\left(\frac{1-\alpha}{\alpha}\right) Q\frac{1}{\alpha} \tag{2}$$

where C is the equivalent capacitance of the constant phase element in parallel with a $R_{CPE}$, Q the constant of the CPE, and $\alpha$ the frequency-dependent constant. The fitted Randles circuit model resulted in $R = 11.9$ kΩ with a deviation of 0.26, $Q = 31.9E\text{-}9$ $Fs^{a-1}$ with a deviation of 96.68E-15, $\alpha = 0.9$ with a deviation of 0.5, and $R_{CPE} = 13.69$ MΩ with a deviation of 24.18. This is then yielding in an equivalent $C_{EDL}$ of 29.2 nF and $R_{EDL}$ of 13.7 MΩ (Figure S1 and Table ST4, Supporting Information). The CPE was used to accurately model the non-ideal capacitive behavior of the electrodes, as indicated by $\alpha = 0.9$, with its equivalent capacitance representing a pseudocapacitive electrode behavior.

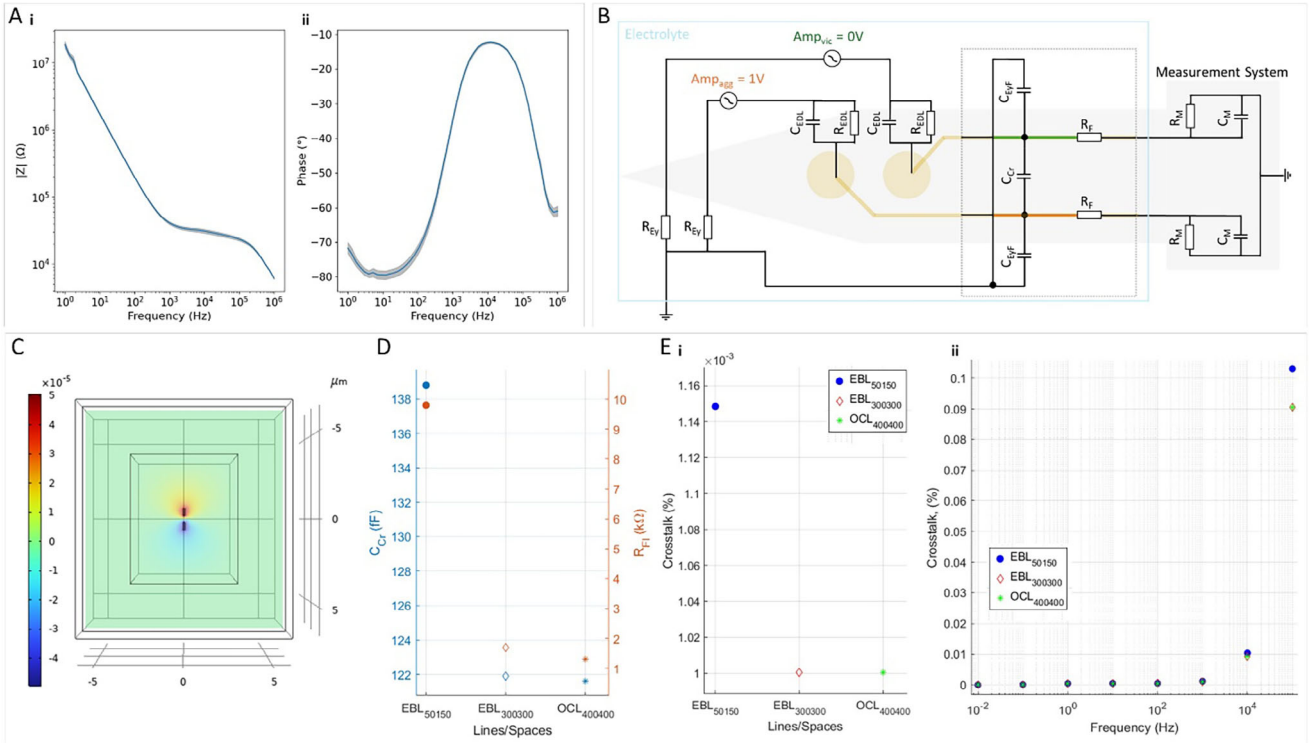


**Figure 2.** Electrical and electrochemical performance. A) Bode plot of the mean (blue) and standard error of the mean (grey shade) of the impedance of three neural implants before their in vivo validation (134 working electrodes). B) Equivalent circuit for crosstalk analysis including the measurement system and an intracortical neural implant, containing the latter an aggressor (orange) and a victim (green) feedline. In the circuit, electrical double layer (EDL) elements such as electrolyte resistance, charge transfer resistance, and electrical double layer capacitance are denoted as $R_{Ey}$, $R_{EDL}$, and $C_{EDL}$, respectively. The measurement setup is represented by $R_M$ and $C_M$, the feedline crosstalk with $C_{CR}$, $C_{EyF}$, and the lead resistance as $R_F$. See details in the main text. C) COMSOL simulation of the distribution of the electric field potential (in volts (V)) for feedlines with 400 nm lines and spaces. D) $C_{Cr}$ (blue) and $R_F$ (orange) for feedline dimensions achieved via EBL and OCT, 50 nm lines and 150 nm spaces ($EBL_{50150}$), 30 nm lines and spaces ($EBL_{300300}$), and 400 nm lines and spaces ($OCL_{400400}$). Calculated crosstalk in percentages Ei) over fabricated feedlines in this work at 1 kHz and Eii) across frequencies.

The Crosstalk simulations were conducted in two steps. First, finite element method (FEM) analysis was used to derive the unknown values of the equivalent circuit of crosstalk between feedlines from the physical 3D-model of the feedline structure (Figure 2B) using COMSOL Multiphysics (COMSOL, Germany). Then, the electrical circuit simulation software EveryCircuit (MuseMaze Inc, USA California) was used to calculate $U_{victim}$ and $U_{aggressor}$ across frequencies using the quantified equivalent circuit of crosstalk between feedlines within the overall equivalent circuit model of the whole measurement setup. The subsequent crosstalk was calculated and visualized using MATLAB (Mathworks Inc., United States) using Equation (1).

For each parameter set of lines and spaces, the components of the equivalent electrical circuit of the feedline structure have been computed in COMSOL using the physical 3D model, which is analyzed as a *black box* (Figure 2A, grey dashed box and Figure S2, Supporting Information) via measurements at its outer terminals, i.e., the ends of the feedlines and an ideal counter electrode to the surrounding electrolyte in the physical 3D-model. The serial lead resistance of the gold feedlines was modeled by resistors $R_F$. The model of the crosstalk behavior between the feedlines was simplified to the direct capacitive coupling between the feedlines ($C_{Cr}$) and the indirect capacitive coupling from the feedlines through their side passivation and the surrounding electrolyte ($C_{EyF}$). To obtain these resistive and capacitive components of the model, a sinusoidal input voltage $u(t)$ of frequency $f$ was generated and fed into the outer terminals of the *black box* in multiple quadripole configurations (Figure S2, Supporting Information). The phase shift ($\varphi$) between voltage and measured current was then calculated according to Equation (3), where $T$ is the time period of $u(t)$ and $\Delta t$ is the time shift between $i(t)$ and $u(t)$.

$$\varphi = 2\pi \frac{\Delta t\ (i,u)}{T} \tag{3}$$

The capacitive values ($C_{cr}$ and $C_{EyF}$) were then calculated according to Equation (4), where $f$ denotes frequency and $|Z|$ the magnitude of the impedance:

$$C = \frac{\sin(\varphi)}{2\pi f\ |Z|} \tag{4}$$

After calculating all values (Tables ST3 and ST4, Supporting Information) for the elements of equivalent circuit of crosstalk, the response of the circuit was simulated in EveryCircuit across frequencies (10 mHz to 100 kHz). Crosstalk was then calculated using Equation (1).

#### 2.2.2. Electrochemical Characterization

An electrochemical impedance spectroscopy (EIS) was performed with A VSP-300 potentiostat (BioLogic Science Instruments, France) to verify the findings of the simulation. Therefore, passivated implants (300LS) on a silicon host wafer were used, where only the contact pads were opened. To contact them electrically two micromanipulators (SÜSS MicroTec) and probes (ST-20-0.5, picoprobe by GGB Industries Inc) were used. In this setup, a contact pad is functioning as a counter and the other as the reference electrode while the feedlines of those are next to each other at the shank. To capture the capacitive behavior the measurement was first performed in air and second with immersing the shank of the implant with 0.1 M PBS using a 10 mV sinusoidal signal with a frequency sweep from 1 Hz to 10 kHz.

The flipped chip bonded implants were characterized by electrochemical impedance spectroscopy (EIS) in a three-electrode setup with the same counter and reference electrodes as previously described and using the electrodes of the implant as working electrodes. A VSP-300 potentiostat (BioLogic Science Instruments, France) was used for EIS measurements in 0.1 M PBS using a 10 mV sinusoidal signal with a frequency sweep from 1 Hz to 1 MHz. Impedances in vivo were measured using Intan RHS 32-channel stim/record headstages (Intan Technologies, USA) at 1kHz.

Thermal noise in microelectrodes results from the random movement of charge carriers within the electrode material, the surrounding electrolyte, or the electrode-electrolyte interface.[34] By calculating the resistance of the fabricated feedline structures an estimation of their performance can be made. The theoretical resistance ($R$) is calculated with:

$$R = \rho \frac{l}{t_{Au} w} \tag{5}$$

where $\rho_{Au}$ = 2.4331e-08 is the specific resistance of gold,[31,32] $l$ = 1863 µm the length of the longest small feedline, a layer-thickness of $t_{Au}$ = 100 nm, and a varying width of $w_{50}$ = 50 nm, $w_{300}$ = 300 nm, $w_{400}$ = 400 nm, $w_2$ = 2 µm, $w_{10}$ = 10µm. The resulting resistances (R) will be used to determine the thermal noise $v_t$ as follows:

$$v_t = \left[4 k_B T R \Delta f\right]^{\frac{1}{2}} \tag{6}$$

With $k_B$ the Boltzmann constant and T = 300 K the absolute temperature and with $\Delta f = f_2 - f_1$ in the frequency range from $f_1$ = 300 Hz to $f_2$ = 3 kHz.

### 2.3. In Vivo Validation

High-density flexible neural implants with submicron feedline resolution were validated in vivo at the University of Cambridge. All animal procedures complied with the UK Animals (Scientific Procedures) Act of 1986. The study received approval from the Animal Welfare and Ethical Review Body at the University of Cambridge and was authorized by the UK Home Office under project license number PFF2068BC and is reported according to the ARRIVE guidelines. Three female Lewis rats were obtained from Charles River Laboratories with a weight of ≈190 g and subsequently maintained for at least seven days of acclimatization at the local animal facility at the University of Cambridge.

#### 2.3.1. Surgical Procedure

Prior to surgery, animals were anesthetized with 5% isoflurane, weighed, and kept under anesthesia at 2.5% isoflurane. Analgesia was given by subcutaneous injection of Metacam (5–10 mg kg$^{-1}$). Fluid replacement was also provided by subcutaneous injection of 2.5 mL 0.9% saline solution. The animals were shaved at the head-neck area and subsequently placed in the surgical area under isoflurane anesthesia at 2.25%. Body temperature was monitored and maintained at 37 °C using a rectal probe and a thermal pad, respectively. Isoflurane was used in a mixture with medical oxygen both pre-operatively and during the surgical intervention.

First, a reference screw (reference electrode) was placed into a trephination hole measuring ≈0.8 mm in diameter above the cerebellum. Subsequently, a craniotomy measuring ≈3.5 mm in diameter was performed at the right hemisphere above the barrel cortex (ML: 5 mm, AP: -2.5 mm from bregma), utilizing a dental drill. The dura was then meticulously removed using a hooked cannula, thereby enabling access to the cortex. Once in place at the desired coordinates, intracortical implantation was carried out and polyethylene glycol (PEG) was dissolved using 0.9% saline solution for a minimum of 15 minutes. Following PEG dissolution, the tungsten rod used as a temporary insertion shuttle was manually removed using surgical forceps, leaving the flexible shank inside the cortex. The shuttle tip was implanted to a depth of 2 mm, allowing the 1.8 mm implant to be fully inserted. The 0.2 mm difference accounts for the shuttle device extending ≈200 µm beyond the implant tip. The implant was externalized from the skull with its corresponding PCB, which was then fixed to the skull using dental cement (Super-Bond Universal Kit, SUN MEDICA Co., LTD, Japan). Implant functionality was first checked with intraoperative electrophysiological recordings under 0.75% isoflurane, followed by the recovery of the animals that lasted for one hour.

#### 2.3.2. In Vivo Electrophysiology

Electrophysiological recordings were conducted using an RHS Stim/Recording System, which was connected to two RHS 32-channel head stages (Intan Technologies, USA). The sampling rate was set at 30 kHz. During the intraoperative recordings, whisker stimulation was carried out by manually brushing the whiskers at 30-second intervals, alternating between the contralateral and ipsilateral sides. Awake recordings were performed on day zero post-implantation, at least one hour after the animals had fully recovered and returned to their home cage. Whisker stimulation on awake rats was conducted by brushing the animal whiskers manually (alternating 30 seconds of whisker

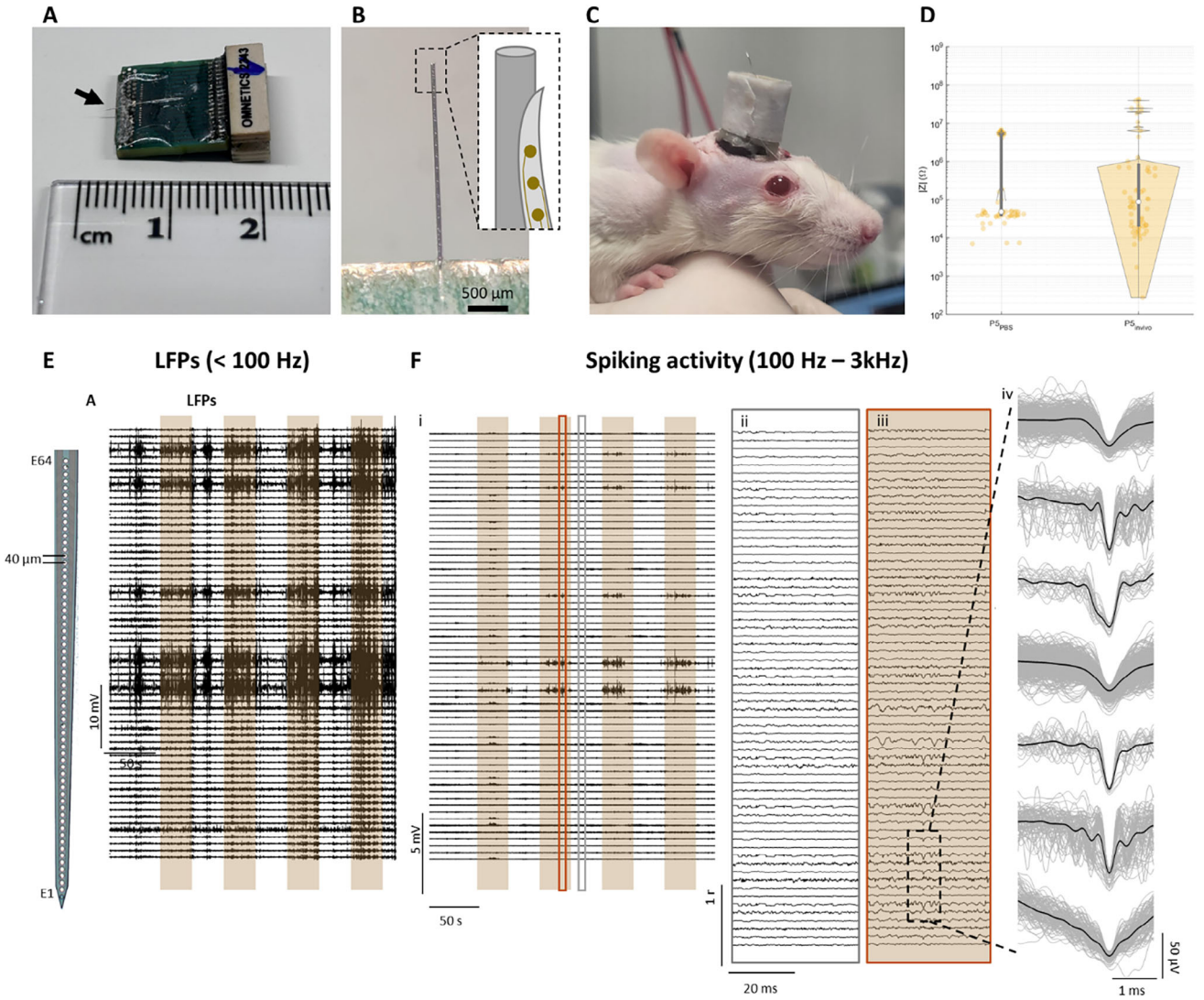


**Figure 3.** In vivo validation of high-density neural implants with submicron feedline resolution. A) High-density single-shank intracortical implant featuring a custom-designed printed circuit board with two 32-channel Omnetics connectors and a temporary stiff insertion shuttle (black arrow). B) Close-up of the flexible intracortical shank temporarily bonded to the stiff insertion shuttle using polyethylene glycol and zoomed-in schematic of how the rod was fixed to the sample at the tip of the implant. C) Awake rat implanted with the high-density intracortical neural implant. D) Electrode impedance comparison measured at 1 kHz in 1× PBS and in vivo. E) Representative LFP, which were low pass filtered (<100 Hz) and Fi) band pass filtered (100 Hz–3 kHz) recording traces showing the captured spiking activity for all 64 channels recorded in an awake rat. Yellow shading indicates 30-second whisker stimulation periods. Insets: neural activity during resting state (Fii) and whisker stimulation (Fiii), along with representative neuronal spike waveforms (Fiv) (the averaged waveform is shown in black and individual spikes in grey).

brushing with 30 seconds of no brushing) for approximately five minutes.

### *2.3.3. Signal Processing*

The data were processed using self-written Matlab (Release R2024, Mathworks Inc., United States) scripts. The raw traces were filtered using a zero-phase 6th-order Butterworth filter. For LFPs, the data were low-pass filtered at 100 Hz, while for spiking activity, the data were band-pass filtered with cut-off frequencies of 100 Hz and 3 kHz. Spike sorting was performed using the UltraMegaSort2000 algorithm.[35] Traces were mapped in order from the most superficial to the deepest electrode within the device and plotted in this order.

## 2.4. Statistical Analysis

Data was analyzed using self-written Matlab (Release R2024, Mathworks Inc., United States) scripts. To show the measured values in Figures 1C and **3D**, the violin plot function by Bastian Bechtold[36] was implemented in the self-written code.

Fifteen measurements were used to create the feedline and space width results (Figure 1Ci-iii). Each point in the graph is one measurement point and the shadow around it is the Kernel

Density Estimation. The critical dimension bias was calculated to distinguish if a feedline width result is harmonizing with the expected width. Therefore, the Equation (5) was used. Here the expected width is divided by the outcomes of 15 measurements of feedlines. To get the deviation, the value was then subtracted from 1 and for percentages multiplied by 100.

$$bias = \left(1 - \left(\frac{width_{expected}}{width_{real}}\right)\right) * 100 \quad (7)$$

The crosstalk-EIS results were plotted with a self-written script in Matlab (Release R2024, Mathworks Inc., United States), and the data from five different measurements in air and 20 measurements in PBS. The data shows a 50 Hz noise (Figure S6, Supporting Information).

To display the EIS results (Figure 2Ai-ii), the data of the three implants for in vivo use were taken. Here the average and standard deviation of all working channels is presented. Therefore, a self-written code in Matlab and Python was used. In these scripts, the working electrodes and non-working ones were sorted by calculating the theoretical impedance using the rationale of the extended Stern model. Afterward, the average, standard deviation, and standard error of the mean of all 134 working channels were determined (Figure S6, Supporting Information). The average is presented as a blue solid line and the standard deviation is a grey shadow around it. For the comparison of the impedance in PBS and in vivo, the impedance data at 1 kHz was extracted and further displayed in a violin plot (Figure 3D).

## 3. Results and Discussion

### 3.1. Lithographic Resolution and Microfabrication of High-Density Neural Implants

With the aim of developing high-density intracortical implants with a minimal cross-sectional footprint, we explored the resolution limits of OCL and EBL to pattern submicron resolution feedlines on thin flexible, and biocompatible polymer substrates, such as parylene-C (PaC). The fabrication process of high-density intracortical probes, which entailed the encapsulation of a single-metal layer with PaC, is outlined in Figure 1A. In this particular instance, the structuring of metal patterns necessitates the patterning of a negative tone photoresist (Figure 1Aiii) that serves as deposition mask for subsequent metal deposition and lift-off (Figure 1Aiv).

#### *3.1.1. Optical Contact Lithography*

Optical Contact Lithography (OCL) is a standard technique in microfabrication and semiconductor processing, particularly in environments where cost-effective, high-throughput patterning is required. However, OCL with a mask aligner fabrication is often challenging due to the physical limitations in resolution in OCL (Table ST2, Supporting Information). Thus, the minimum feature size achievable at our facility, given a broadband wavelength range of 345 to 460 nm (see Experimental Section) is ≈500 nm.[37] However, by optimizing the process parameters, we successfully fabricated lines and spaces patterns of 330 and 440 nm in the photoresist, respectively (Figure S3A, Supporting Information). Nonetheless, metal lift-off within those or lower photoresist dimensions proved to be challenging (Figure S3B, Supporting Information).

In the context of process parameter optimization, the selection of photoresist and its height are of paramount importance, as both factors exert a substantial influence on the thickness of the deposited metal layer that is deemed feasible. In conjunction with other process parameters, such as the post-exposure bake of negative tone photoresist, the photoresist undercut can be tuned. This, in turn, plays a crucial role in achieving a successful lift-off process without photoresist residues or unwanted residual metal structures (known as fencing).[38] In this regard, diluted AZ LNR-003 (EBR:LNR003) demonstrated the most optimal undercut with less C-shape distortion in its cross-section, in contrast to other negative or image reversal photoresists, which exhibited distorted C-shaped undercuts that are susceptible to metal lift-off failure (Figures S3 and S4, Supporting Information).

Following a thorough exploration of process parameters, we achieved a photoresist structure height of ≈730 nm, which is 6-fold thicker than our standard metal layer stack of 20 nm of Titanium and 100 nm of gold. With this layer stack, the metal lift-off in NI555 was feasible, yielding final fabricated metal feedlines 520 nm wide with a space of 280 nm (Figure 1Bi,Ci). In Figure 1Bi-ii the dimensions of the fabricated feedlines and spaces ($N = 15$ feedlines) were extracted from different FIB-cuts (FEI TFS Helios 600i G3), resulting in a critical dimension bias of 20–35 %, corresponding to 120 nm dimensional deviation of the resulting structures from the mask. This outcome attained the resolution limit of OCL, given that the mask dimensions (400 nm) match the UV exposure wavelength of the mask aligner at our facility.

The feedline miniaturization achieved in this study surpasses the ones reported in the literature, particularly when one considers the possibility of designing a high-density intracortical shank with one metal layer embedded in a polymer substrate (Table ST1, Supporting Information). This approach has the potential to reduce microfabrication complexity and processing time. While submicron feedline resolution has been accomplished, high-density sub-50 µm shank widths with single metal layers remain unfeasible with OCL and broadband exposure, given that a minimum shank width of 51 µm is required for a 64-channel shank containing 64 feedlines, without considering the electrodes and side space. To further enhance feedline resolution in OCL, the UV wavelength can be reduced by implementing optical filters or using deep UV lithography. Additionally, in our tests, antireflective coatings were useful in suppressing any reflection from the surface of the substrate and hence hindered the resist to form a C-shape undercut profile (Figure S5, Supporting Information). This process allowed an easy lift-off after metallization, but could not realize a coating that is suitable in the overall process and for the purpose of the feedlines.

#### *3.1.2. Electron-Beam Lithography*

EBL is known for its high alignment and structure accuracy. Its limiting factors do not arise from the technique itself in

comparison to OCL; rather they arise from the processing of the substrate material, in this case, PaC itself, for two primary reasons. First, most common EBL-resists need to be developed by solvents, which, however, can cause swelling, alter the properties of PaC, or degrade it, since it is sensitive to solvents.[39] Furthermore, a suitable undercut is in our experience always a challenge on PaC, but it is crucial for a working lift-off process as discussed before.

We therefore conducted a series of experiments with different solvents to our processes. To create a well-defined undercut, we tested a double-layer stack of a copolymer (AR-P617.03)[17] and PMMA (AR-P679.03)[18] or CSAR (AR-P6200.03)[40] as proposed by Allresist GmbH. The Copolymer resist is a suitable choice for the first layer in a double-layer stack due to its higher electron sensitivity compared to PMMA or CSAR. This increased sensitivity allows the copolymer to develop more quickly than the top PMMA or CSAR layer, resulting in a well-defined undercut after development (Figure 1Aviii). Usually, for EBL down to a few nanometers, CSAR is preferred due to its high contrast and process stability. However, using AR 600-546 as developer left residues on the feedlines as well as on the contact pads making the subsequent lift-off problematic. Finally, the copolymer AR-P 617.03 and PMMA AR-P 679.03 showed the most promising results using a methyl isobutyl ketone (MIBK)-based developer (AR 600–55) especially after introducing a cold development method at 0 °C for increasing the contrast of the PMMA.[20,21,41] With this process, we were able to achieve average metal feedlines down to 50 nm and a spacing of 150 nm (50/150 LS), as well as 320 nm lines and 280 nm spacing (300 LS) (Figure 1Ciii–v). Finally, the copolymer AR-P 617.03 and PMMA AR-P 679.03 showed the most promising results using a methyl isobutyl ketone (MIBK)-based developer (AR 600–55) especially after introducing a cold development method at 0 °C for increasing the contrast of the PMMA.[20,21,41] With this process, we were able to achieve average metal feedlines down to 50 nm and a spacing of 150 nm (50/150 LS), as well as 320 nm lines and 280 nm spacing (300 LS) (Figure 1Ciii–v).

#### 3.1.3. Challenges

In addition to resolution-related challenges, substrate particles can compromise the adhesion of both photoresist and metal layer stack, leading to an imperfect lift-off mask, failed metal lift-off, or disrupted feedlines in both lithography techniques. In OCL, non-optimal exposure doses or photoresist inhomogeneities can result in poor undercutting, causing fencing effects (photoresist residues) or disrupted feedlines. In EBL, structures are written within write fields (WF), where the electron beam is shifted along a small area on the sample. Once the writing is done in this WF, the stage moves to the next WF. Due to misalignment of the electron beam or stage inaccuracies, beam stitching errors can occur yielding an offset in the feedlines at the WF boundary and hence to failures in the lift-off procedure.[42] Additionally, in EBL, fine and coarse structures are patterned separately, and thermal drifts over long exposures can cause misalignments, further compromising the lift-off mask. These challenges are particularly critical for the microfabrication of long, narrow feedlines. However, the process flows presented in this work enabled the successful fabrication of feedlines as narrow as 40 nm and as long as 1863 µm.

#### 3.1.4. High-Density Neural Implant with Submicron Resolution

After exploring the resolution limits and despite the challenges of OCL and EBL for the patterning of the deposition mask for metal lift-off, we microfabricated functional high-density neural implants with a single metal layer process and housing 64 electrodes with a diameter of 12.5 µm and a pitch of 40 µm in one intracortical 1.8 mm long shank. Toward cross-sectional miniaturization, two shank designs with a narrowing cross-section toward the tip were implemented using EBL. The first design featured a maximum shank width of 50 µm, comprising 50 nm lines and 150 nm spaces (see Figure 1Di–iii). The second design exhibited a maximum shank width of 70 µm, with 300 nm lines and spaces (see Figure 1Dii,iv). Both shank designs feature a narrow shank width toward the tip of only 35 µm.

### 3.2. Electrical and Electrochemical Performance

Neural implants aim to interact with nervous tissue and detect extracellularly neural activity, which lies at the microvolt range. Therefore, their electrical and electrochemical performance is critical for recording quality. Due to the reduced feedline dimensions proposed in this work, both the impedance of working electrodes and crosstalk are key factors influencing the functionality of these devices.[43,44]

#### 3.2.1. Electrochemical Performance

The electrodes of the high-density intracortical implants containing 300 nm feedlines were coated with PEDOT:PSS, exhibiting an average impedance at 1 kHz of 40.8 kΩ with a standard deviation error of the mean of 2.1 kΩ ($N$ = 134 working electrodes across three implants) (Figure 2Ai; Figure S6, Supporting Information). The electrodes showed capacitive behavior at higher frequencies and a resistive behavior at lower frequencies, typical of PEDOT:PSS electrodes.[45] Their low impedance rendered them suitable for neural recording.[44] (Figure 2A). The electrical continuity of the feedlines was confirmed in finalized devices with 300 nm-wide feedlines (lines and spaces), as successful electrodeposition of PEDOT:PSS was verified through electrochemical impedance measurements. This demonstrated continuity for a 300 nm-wide, 1863 µm-long feedline.

#### 3.2.2. Crosstalk

Due to the miniaturized dimension of the feedlines and their proximity, both in the nanometer range, crosstalk was evaluated. Crosstalk is defined as the unintended interference, also known as coupling, between adjacent conductive pathways, in this context, feedlines.[24] Hence, crosstalk is the most significant technical limitation for scaling up the electrode count for high-density microelectrode arrays for neural recording, as it implies scaling

down the dimensions of feedlines, which are then susceptible to two primary forms of crosstalk: capacitive, characterized by the induction of unintended voltages on neighboring feedlines, and resistive, marked by direct current leaks.

To investigate the effects of feedline dimensional miniaturization on crosstalk, we proposed an equivalent circuit to model the expected measurement configuration (Figure 2B). The circuit is composed of two primary components: one that is submerged in an electrolyte solution and one that is exposed to ambient air. The latter component primarily consists of the recording system connected to neural implants. In turn, the first block comprehends a shank with two gold/PEDOT:PSS working electrodes with a diameter of 12.5 µm, each connected to 1.8 mm long gold feedlines, with varying widths and inter-spacing and separated by an insulating material (PaC). Both electrodes and feedlines are immersed in an electrolyte, resembling the setup of an intracortical neural implant. Hence, in our region of interest (Figure 2B, *black box*, dashed grey box), each feedline is represented by the lead resistance $R_F$, and the influence of crosstalk was modeled with two capacitors, $C_{cr}$ and $C_{EyF}$, representing the direct capacitive coupling between adjacent feedlines, as well as the indirect coupling between the feedlines, the side passivation, and electrolyte, respectively.

FEM analysis visualized the electric field potential between feedlines during electrical recording. The distribution of the electric field potential shows that the active feedline (aggressor) introduces an electric potential into the passive feedline (victim), which is the discussed crosstalk effect (Figure 2C). The results of the FEM simulation show a capacitive coupling in the fF-range, which is consistent with previous studies of crosstalk in polymer-based microelectrode arrays.[46]

As anticipated, capacitive coupling and lead resistance increase for submicron feedline structures (Figure 2D). Accordingly, we expect an approximately 13-fold increase in thermal noise when comparing a 50 nm ($v_{t50}$ = 0.67 µV) wide feedline with a 10 µm ($v_{t10000}$ = 0.05 µV) wide feedline. However, even for the smallest fabricated feedline in this work, (Table ST6, Supporting Information), thermal noise remains below 1 µV and below 0.5 µV for a 300 nm wide feedline ($v_{t300}$ = *0.26* µV), which was used for our in vivo validation, indicating minimal impact on electrophysiological recordings. Additionally, circuit simulation across frequencies predicted minimal crosstalk. Even the smallest feedline structure with a width of 50 and 150 nm spacing exhibited crosstalk of only 0.0011% at 1 kHz, the frequency of interest for the recording of neuronal APs[47] (Figure 2Eii). A trend of higher crosstalk at higher frequencies was obtained, as expected (Figure 2Eii). In order to achieve high-quality neuronal recordings, crosstalk should not exceed 1%.[43] Consequently, we do not anticipate significant crosstalk in any of the feedline structures that are presented in this study. Therefore, these structures are deemed suitable for neuronal recordings.

The validation of the crosstalk model was attempted using electrochemical impedance spectroscopy on passivated electrodes (covered with PaC) with adjacent submicron feedlines (300 nm lines and spaces). Measurements were conducted in air to assess direct crosstalk capacitance ($C_{cr}$) and in PBS to account for both direct ($C_{cr}$) and indirect ($C_{EyF}$) capacitances. While impedance measurements in air showed lower capacitance than those in PBS, the results are considered unreliable. At lower frequencies (below 100 Hz), the measured impedances fall outside the specifications of the measuring devices, and at higher frequencies (above 100 Hz and up to 1 MHz), accuracy decreases with deviations of up to 1%, making it difficult to accurately fit the system (Figure S6, Supporting Information).

### 3.3. In Vivo Validation

Flexible high-density intracortical implants with submicron resolution were validated in vivo in rats. After the microfabrication, we integrated the flexible implants with a customized and miniaturized front-end connector, characterized by a form factor of 12 mm × 17 mm, and a total weight of 0.9 g. The lightweight nature of the implants rendered them suitable for in vivo applications in small animal models, such as rats (Figure 3A). Subsequently, a stiff shuttle, consisting of a 50 µm-tungsten rod, was temporarily affixed onto the flexible intracortical shank to aid the insertion of the implant (Figure 3B) and removed after dissolving the PEG-based adhesive intraoperatively.

To assess the functionality of the devices, we monitored the impedance of recording electrodes in vivo, both intraoperatively and during awake recordings. An illustrative representation of the electrode impedance distribution is presented in Figure 3D, where the majority of the electrodes exhibited an impedance at 1 kHz below 1 MΩ (Figure 3D; Figures S8 and S9, Tables ST7 and ST8, Supporting Information), thereby confirming their suitability for neuronal recording. The average impedance magnitude at 1 kHz was 127 kΩ ($N$ = 91 electrodes across three probes) with a standard error of 20 and 139 kΩ ($N$ = 78 electrodes across three probes) with a standard error of 23 kΩ intraoperatively and in awake recordings, respectively. Electrode survival rates ranged from 87 to 98% in two of the three implanted animals but dropped to 9% in the third implant during intraoperative monitoring, with further reductions during awake recordings. For example, the percentage of functional electrodes in the first probe decreased from 87% to 55%. In the third implant, immediate intraoperative failure occurred due to physical damage from the removal of the insertion shuttle.

The large spread of the in vivo impedances toward the MΩ range (Figure 3D; Figures S8 and S9, Tables ST7 and ST8, Supporting Information) suggests that the PEDOT:PSS electrode coating might have been compromised during insertion, leading to increased electrode impedances. Additionally, incorrect classification of electrodes as non-functional electrodes can be also affected due to loose connections between the implants and the head stage or to undissolved PEG from the recording sites during intraoperative recordings. This may explain why the second implant exhibited a higher number of functional recording electrodes during awake recordings compared to intraoperative impedance measurements (Tables ST7 and ST8, Supporting Information).

Since the implants were positioned in the barrel cortex, we performed whisker brushing in awake animals to trigger cortical neuronal activity. We utilized the high-density electrode array to characterize activity across cortical layers. Both lower-frequency recordings containing local-field potentials (LFPs) (Figure 3E) and higher-frequency recordings containing neuronal spikes (Figure 3F) showed increased activity during whisker brushing.

This activity was particularly visible at certain depths along the electrode array, suggestive of cortical layer-specific recordings. Particularly high amplitude recordings were observed in channels at depths of 1.3 to 1.5 mm into the cortex, likely corresponding to layer 5 neurons (Figure 3E,F). This approach also enabled the simultaneous recording of multiple neuronal units across electrodes, as confirmed by representative spike waveforms from electrodes located in the deepest cortical layers.

## 4. Conclusion

In this study, we explored the fabrication limits of OCL and EBL on polymeric substrates to advance high-density, flexible neural implants for neurophysiology. Our objective was to realize high-density intracortical shank designs with a small footprint while achieving a higher channel count, to enable large-scale neuronal recordings. Given its established biocompatibility and conformability, PaC was selected as the substrate and encapsulation material to ensure stable integration within neural tissue.

By testing the technical limitations of OCL, we successfully fabricated submicron metal feedlines with widths of 520 nm and spaces of 280 nm on PaC, exceeding the minimum feature size of 600 nm reported by others on polymer substrates.[6] Further improvements using EBL enabled the realization of ultra-high-density feedlines down to 50 nm, with interconnect spaces as small as 150 nm. These outcomes demonstrate the feasibility of miniaturization while reducing manufacturing complexity, enabling the implementation of high-density single-metal layer devices and further high-density multi-shank and multi-site neural implants. The advancements in fabrication technology facilitated the development of a 64-channel neural implant with a 1.8 mm long shank with a cross-section of 6 µm × 50–70 µm (300-420 µm$^2$), demonstrating a density of 507–711 electrodes per mm$^2$.

To assess the performance of the devices, both electrochemical and electrical properties were investigated through theoretical simulations and impedance spectroscopy in PBS and in vivo conditions, demonstrating low impedance PEDOT:PSS-based electrodes with submicron feedline providing minimal crosstalk. Finally, the in vivo validation of the fabricated implants confirmed their ability to record neuronal activity across cortical layers, demonstrating their potential for both acute and chronic neurophysiological applications. These results highlight the feasibility of using OCL and EBL for fabricating next-generation neural interfaces with enhanced resolution and reduced invasiveness.

## Supporting Information

Supporting Information is available from the Wiley Online Library or from the author.

## Acknowledgements

The authors thank the Helmholtz Nano Facility (HNF) at *Forschungszentrum* Jülich for facilitating the microfabrication of the devices. The authors also thank the Bioelectronics Laboratory at the University of Cambridge for facilitating the in vivo validation of the devices. The authors thank B. Breuer for organizational support, E. Brauweiler-Reuters for carrying out SEM, and M. Prömpers, M. Banzet, and R. Stockmann for technical support at the HNF. This work was supported by the Deutsche Forschungsgemeinschaft (DFG, German Research Foundations; GRK2610 – project number 424556709).

## Conflict of Interest

The authors declare no conflict of interest.

## Author Contributions

L.K. and V.R.M. conceived the development of high-density flexible intracortical implants and planned the study. L.K. fabricated the devices with the support of T.G, E.Y, S.D, M.Kasavetov, A.O., and V.R.M. L.K., S.D., E.Y. and M.Kasavetov characterized the devices with the support of V.R.M. Crosstalk simulations were carried out by L.K. and M.Kleutgens with the support of E.Y, M.Kasavetov, A.O, and V.R.M. In vivo validation was carried out by A.C.L. and V.R.M. with the support of G.M. Electrophysiological data was processed by M.J. with the support of V.R.M. L.K. collected and processed microfabrication and characterization data and processed figures with the support of M.J. and V.R.M. L.K. and V.R.M. wrote the initial draft of the manuscript. All authors reviewed and edited the manuscript. V.R.M. supervised the project.

## Data Availability Statement

The data that support the findings of this study are available from the corresponding author upon reasonable request.

## Keywords

flexible neural implants, high-density, intracortical implants, microelectrode arrays, neurotechnology

Received: January 31, 2025
Revised: March 19, 2025
Published online: April 23, 2025

[1] T. Stieglitz, *Neuroethics* **2021**, *14*, 5.
[2] A. Cometa, A. Falasconi, M. Biasizzo, J. Carpaneto, A. Horn, A. Mazzoni, S. Micera, *iScience* **2022**, *25*, 105124.
[3] A. Carnicer-Lombarte, S.-T. Chen, G. G. Malliaras, D. G. Barone, *Front. Bioeng. Biotechnol.* **2021**, *9*, 622524.
[4] M. Vomero, F. Ciarpella, E. Zucchini, M. Kirsch, L. Fadiga, T. Stieglitz, M. Asplund, *Biomaterials* **2022**, *281*, 121372.
[5] L. Luan, R. Yin, H. Zhu, C. Xie, *Annu. Rev. Biomed. Eng.* **2023**, *25*, 185.
[6] X. Yang, T. Zhou, T. J. Zwang, G. Hong, Y. Zhao, R. D. Viveros, T.-M. Fu, T. Gao, C. M. Lieber, *Nat. Mater.* **2019**, *18*, 510.
[7] A. Sharon, M. M. Jankowski, N. Shmoel, H. Erez, M. E. Spira, *Acta Biomater.* **2023**, *158*, 292.
[8] J. Abu Shihada, M. Jung, S. Decke, L. Koschinski, S. Musall, V. Rincón Montes, A. Offenhäusser, *Adv. Sci.* **2024**, *11*, 2305944.
[9] V. R. Montes, J. Gehlen, S. Ingebrandt, W. Mokwa, P. Walter, F. Müller, A. Offenhäusser, *Sci. Rep.* **2020**, *10*, 19836.
[10] K. Joseph, M. Kirsch, M. Johnston, C. Münkel, T. Stieglitz, C. A. Haas, U. G. Hofmann, *Biomaterials* **2021**, *279*, 121230.
[11] C. M. Tringides, N. Vachicouras, I. de Lázaro, H. Wang, A. Trouillet, B. R. Seo, A. Elosegui-Artola, F. Fallegger, Y. Shin, C. Casiraghi, K. Kostarelos, S. P. Lacour, D. J. Mooney, *Nat. Nanotechnol.* **2021**, *16*, 1019.
[12] N. A. Steinmetz, C. Aydin, A. Lebedeva, M. Okun, M. Pachitariu, M. Bauza, M. Beau, J. Bhagat, C. Böhm, M. Broux, S. Chen, J. Colonell, R. J. Gardner, B. Karsh, F. Kloosterman, D. Kostadinov, C. Mora-Lopez, J. O'Callaghan, J. Park, J. Putzeys, B. Sauerbrei, R. J. J. van Daal, A. Z. Vollan, S. Wang, M. Welkenhuysen, Z. Ye, J. T. Dudman, B. Dutta, A. W. Hantman, K. D. Harris, et al., *Science* **2021**, *372*, abf4588.

[13] E. Musk, Neuralink, *J. Med. Internet Res.* **2019**, *21*, 16194.
[14] C. Böhler, M. Vomero, M. Soula, M. Vöröslakos, M. Porto Cruz, R. Liljemalm, G. Buzsaki, T. Stieglitz, M. Asplund, *Adv. Sci.* **2023**, *10*, 2207576.
[15] X. Wei, L. Luan, Z. Zhao, X. Li, H. Zhu, O. Potnis, C. Xie, *Adv. Sci.* **2018**, *5*, 1700625.
[16] W. Albrecht, J. Moers, B. Hermanns, *J. Large-Scale Res. Facil. JLSRF* **2017**, *3*, A112.
[17] "product information: positive e-beam resists AR-P 610 series"; Allresist. https://www.allresist.com/wp-content/uploads/sites/2/2020/03/AR-P610_english_Allresist_product-information.pdf (accessed: January 2025).
[18] "product information: positive PMMA E-Beam Resists AR-P 630 – 670 series"; Allresist. https://www.allresist.com/wp-content/uploads/sites/2/2024/12/Allresist_Product-information-E-Beamresist-AR-P-630-670-English-web.pdf (accessed: March 2025).
[19] B. Sun, T. Grap, T. Frahm, S. Scholz, J. Knoch, *J. Vac. Sci. Technol. B, Nanotechnol. Microelectron. Mater. Process. Meas. Phenom.* **2021**, *39*, 052601.
[20] B. Cord, J. Lutkenhaus, K. K. Berggren, *J. Vac. Sci. Technol. B, Microelectron. Nanometer Struct. Process. Meas. Phenom.* **2007**, *25*, 2013,.
[21] W. Hu, G. H. Bernstein, K. Sarveswaran, M. Lieberman, presented at *2003 Third IEEE Conf. on Nanotechnology, 2003. IEEE-NANO 2003.*, San Francisco, CA, USA, July **2003**.
[22] K. Srikantharajah, "Development, characterization, and application of compliant intracortical implants," RWTH Aachen. https://publications.rwth-aachen.de/record/836520/files/836520.pdf.
[23] D. Berman, J. Krim, *Thin Solid Films* **2012**, *520*, 6201.
[24] Y. Qiang, W. Gu, Z. Liu, S. Liang, J. H. Ryu, K. J. Seo, W. Liu, H. Fang, *Nano Res.* **2021**, *14*, 3240.
[25] V. J. Bhat, D. Blaschke, E. Müller, R. Ehricht, H. Schmidt, *Biosensors* **2023**, *13*, 841.
[26] A. Angulo-Sherman, H. Mercado-Uribe, *Chem. Phys. Lett.* **2011**, *503*, 327.
[27] "ME2100-HS32-M 32 Multi Channel Systems", https://www.multichannelsystems.com.sites/multichannelsystems.com/files/documents/data_sheets/MCS_ME2100-HS32-M_Datasheet.pdf (accessed: January 2025).
[28] "Parylene Dielectric Properties.", https://scscoatings.com/newsroom/blog/parylene-dielectric-properties/ (accessed: March 2025).
[29] "S. C. S. P. properties.", Special Coating Systems, https://scscoatings.com/technical-library/en/download/2249/?tmstv=1738237248 (accessed: January 2025).
[30] W. S. Choi, S. S. A. Seo, K. W. Kim, T. W. Noh, M. Y. Kim, S. Shin, *Phys. Rev. B* **2006**, *74*, 205117.
[31] R. A. Matula, *J. Phys. Chem. Ref. Data* **1979**, *8*, 1147.
[32] H. J. Kim, S. Kim, S. Kim, S. Kim, K. Heo, J.-H. Lim, H. Yashiro, H.-J. Shin, H.-G. Jung, Y. M. Lee, S.-T. Myung, *Adv. Mater.* **2024**, *36*, 2308592.
[33] A. Lasia, *J. Phys. Chem. Lett.* **2022**, *13*, 580.
[34] M. Mierzejewski, H. Steins, P. Kshirsagar, P. D. Jones, *J. Neural Eng.* **2020**, *17*, 052001.
[35] D. N. Hill, S. B. Mehta, D. Kleinfeld, *J. Neurosci.* **2011**, *31*, 8699.
[36] B. Bechthold, violinplot.m, https://github.com/bastibe/Violinplot-Matlab/blob/master/violinplot.m.
[37] J. Knoch, Nanoelectronics Device Physics, Fabrication, Characterization, De Gruyter Studium **2024**, https://doi.org/10.1515/9783111054421.
[38] K. Cheng, *IEEE Trans. Semicond. Manuf.* **2020**, *33*, 564.
[39] H. C. Koydemir, H. Kulah, C. Ozgen, *J. Microelectromechanical Syst.* **2014**, *23*, 298.
[40] "Product information: positive e-beam resists AR-P 6200 (CSAR 62)." Allresist, https://www.allresist.com/wp-content/uploads/sites/2/2020/03/AR-P6200_CSAR62english_Allresist_product-information.pdf (accessed: January 2025).
[41] L. E. Ocola, A. Stein, *J. Vac. Sci. Technol. B, Microelectron. Nanometer Struct. Process. Meas. Phenom.* **2006**, *24*, 3061.
[42] R. K. Dey, B. Cui, *J. Vac. Sci. Technol. B, Nanotechnol. Microelectron. Mater. Process. Meas. Phenom.* **2013**, *31*, 06F409.
[43] N. Pérez-Prieto, M. Delgado-Restituto, *Front. Neurosci.* **2021**, *15*, 681085.
[44] C. M. Lewis, C. Boehler, R. Liljemalm, P. Fries, T. Stieglitz, M. Asplund, *Adv. Healthcare Mater.* **2024**, *13*, 2303401.
[45] M. Ganji, A. T. Elthakeb, A. Tanaka, V. Gilja, E. Halgren, S. A. Dayeh, *Adv. Funct. Mater.* **2017**, *27*, 1703018.
[46] S. A. Nikles, D. S. Pellinen, J. Kitagawa, R. M. Bradley, D. R. Kipke, K. Najafi, in *Proceedings of the 25th Annual Int. Conf. of the IEEE Engineering in Medicine and Biology Society (IEEE Cat. No.03CH37439)*, IEEE, Piscataway, NJ, **2003**, pp. 3340–3343.
[47] M. E. J. Obien, K. Deligkaris, T. Bullmann, D. J. Bakkum, U. Frey, *Front. Neurosci.* **2015**, *8*, 423.